High Entropy Bi – Ti Alloying for Improved $Sb_2Si_2Te_6$ Thermoelectrics

Kivanc Saglik, Xizu Wang, Xian Yi Tan, Jinfeng Dong, Ping Luo, Qiang Zhu, Ady Suwardi, Qingyu Yan*

K. Saglik, X.Y.Tan, J.Dong, Q. Yan
School of Materials Science and Engineering, Nanyang Technological University, 50 Nanyang Ave, Block N4.1, Singapore 639798, Republic of Singapore
E-mail: alexyan@ntu.edu.sg

K. Saglik, X.Wang, X.Y.Tan, P. Luo, Q. Zhu
Institute of Materials Research and Engineering (IMRE)
Agency for Science, Technology, and Research (A*STAR), 2 Fusionopolis Way, Singapore 138634, Republic of Singapore

Q. Zhu
Institute of Sustainability for Chemicals, Energy and Environment ($ISCE^2$), Agency for Science, Technology, and Research (A*STAR), 1 Pesek Road, Jurong Island, 627833, Singapore

A.Suwardi
Department of Electrical Engineering, The Chinese University of Hong Kong (CUHK), Central Ave, Hong Kong, 999077

* Corresponding author

Keywords: ($Sb_2Si_2Te_6$, layered thermoelectrics, high entropy alloying, thermoelectricity, doping.)

Conflicts of interest

The authors state that there are no conflicts to declare.

Data availability

The data supporting this article have been included as part of the supplementary information.

Abstract

$A_2B_2Te_6$ type materials attract significant interest due to their layered structures and inherently low thermal conductivity, but their low electrical conductivity limits their thermoelectric performance. High entropy alloying has emerged as an effective strategy to enhance electrical conductivity while preserving low thermal conductivity. This study introduces a two-step high-entropy alloying approach in $Sb_2Si_2Te_6$ where Bi/Ti co-alloying optimizes the carrier concentration and reduces thermal conductivity. Pisarenko plot analysis reveals a substantial increase in effective mass for $Sb_{1.5}Bi_{0.5}Si_{1.6}Ti_{0.3}Te_6$, resulting in a stable Seebeck coefficient of 210 μVK^{-1}, and a power factor of 700 $\mu Wm^{-1}K^{-2}$ between 773 – 873 K. At 673 K, lattice thermal conductivity drops to 0.26 $Wm^{-1}K^{-1}$ at 673 K, approaching the amorphous limit, due to enhanced alloy scattering, point defect scattering, and dislocations as confirmed by SEM and TEM analyses. Jonker plot analysis demonstrates minimal degradation in electrical properties despite the significant reduction in lattice thermal conductivity, improving the quality factor. The combination of optimized Fermi level and reduced thermal conductivity leads to a zT (thermoelectric figure of merit) plateau of 1.11 between 623 -723 K with an average zT of 0.68. These results highlight the potential of high-entropy alloying in advancing layered thermoelectric materials.

1. Introduction

Thermoelectric materials have attracted significant attention due to their ability to convert waste energy, which constitutes about 60% of the energy produced in industrial and residential processes, into useful power.[[1]] The power conversion efficiencies (PCE, η) of thermoelectric devices depend on materials' thermoelectric figure of merit, zT, formulated as: $zT = (S^2 \sigma / \kappa)T$, where S, σ, κ, and T represent the Seebeck coefficient, electrical conductivity, thermal conductivity, and temperature, respectively.[[2]] For thermoelectric technology to compete with existing power generation systems, a zT value greater than 4 is required.[3] However, the advancements in zT are constrained by the inverse relationship between electrical and thermal conductivities, which are both influenced by carrier concentration, n. Consequently, ideal thermoelectric materials typically exhibit a carrier concentration in the range of 10^{19}–10^{20} cm^{-3}. [4] To enhance zT, efforts have been focused on decoupling thermoelectric transport properties. Such strategies include band engineering [5-11] to boost the power factor, while lattice thermal conductivity is reduced through approaches such as nanostructuring,[12, 13] defect engineering,[14, 15] the implementation of all-scale hierarchical microstructures,[16-19] texturing,[20] and the use

of materials with complex crystal structures.[21-23] Owing to the these advancements, space-crafts,[2] wearables,[24, 25] and vehicles[14] are potential application areas of thermoelectric technology.

Thermoelectric materials could be utilized across low, medium, or high temperatures depending on their bandgap. Recently, $A_2B_2Q_6$ family (A: Sb, Bi, Sc, Cr; B: Si, Ge; Q: Te, Se) has emerged as a promising class of medium-temperature thermoelectric materials due to their intrinsically low thermal conductivity arising from their layered structures.[26, 27] Experimental studies on $In_2Ge_2Te_6$ and $Cr_2Ge_2Te_6$ have shown that both materials possess low thermal and electrical conductivities, which limit their zT values to a maximum of 0.5. [26, 28] Among $A_2B_2Q_6$ compounds, $Sb_2Si_2Te_6$ stands out as the composition with the highest peak zT value of 1.08 at 823K, both as a bulk material and in monolayer form. [8, 29] This material features a layered structure consisting of $SbTe_6$ octahedra and Si_2Te_6 ethane-like units. [8] The anisotropy in bonding strength within this layered structure contributes to $Sb_2Si_2Te_6$'s intrinsically low lattice thermal conductivity.

Compared to the conventional state of art Bi_2Te_3-based thermoelectric materials, $Sb_2Si_2Te_6$ offers some important advantages. For instance, $Sb_2Si_2Te_6$ has a larger bandgap (0.6 eV[8]) than Bi_2Te_3 (0.15[30] eV), which suppresses minority carrier excitation and makes it more suitable for medium-temperature power generation applications. Additionally, $Sb_2Si_2Te_6$ has a larger Grüneisen parameter (2.14-4.4[31]) compared to Bi_2Te_3 (0.2-1.8[32]), and $Bi_{0.5}Sb_{1.5}Te_3$ (2.3[33]), which helps lower its lattice thermal conductivity.

$Sb_2Si_2Te_6$ and $Bi_2Si_2Te_6$ share the same crystal structure, with $Bi_2Si_2Te_6$ expected to have lower thermal conductivity due to the heavier Bi atoms substituting Sb. However, $Sb_2Si_2Te_6$ exhibits lower thermal conductivity, primarily governed by its large Grüneisen parameters and the presence of V_{Sb} vacancies, which serve as phonon scattering centers. Additionally, these V_{Sb} vacancies are the main contributors to $Sb_2Si_2Te_6$'s high carrier concentration of $6x10^{-19}$ cm^{-3}.[34] The larger electronegativity of Sb also results in a wider bandgap compared to $Bi_2Si_2Te_6$, leading to a relatively large Seebeck coefficient of 120 μVK^{-1}. This combination of a higher Seebeck coefficient, optimal carrier concentration, and low lattice thermal conductivity enables $Sb_2Si_2Te_6$ to outperform $Bi_2Si_2Te_6$. Consequently, doping Sb on the Bi sites of $Bi_2Si_2Te_6$ increases carrier concentration, reduces thermal conductivity, and enhances the overall thermoelectric figure of merit[35].

The intrinsically low thermal conductivity of $Sb_2Si_2Te_6$ was further reduced through a Te-assisted SPS process, where the formation of Si_2Te_3 nanosheets increased the Seebeck

coefficient, resulting in a *zT* of 1.65 at 823 K.[8] Doping with Ge[36], Mg,[37] Ca[38], and Y[39] introduced point defects, such as Mg_{Sb}^{-} and Ca_{Sb}^{-} which led to increased carrier concentration and further lowered lattice thermal conductivity. Additionally, $Sb_2Si_2Te_6$ was found to enhance the phonon scattering in $Bi_{0.4}Sb_{1.6}Te_3$, thereby boosting its *zT* to 1.3 at 375 K.[40] A summary of the thermoelectric performance enhancements of all $Sb_2Si_2Te_6$ materials is presented in Figure 1.

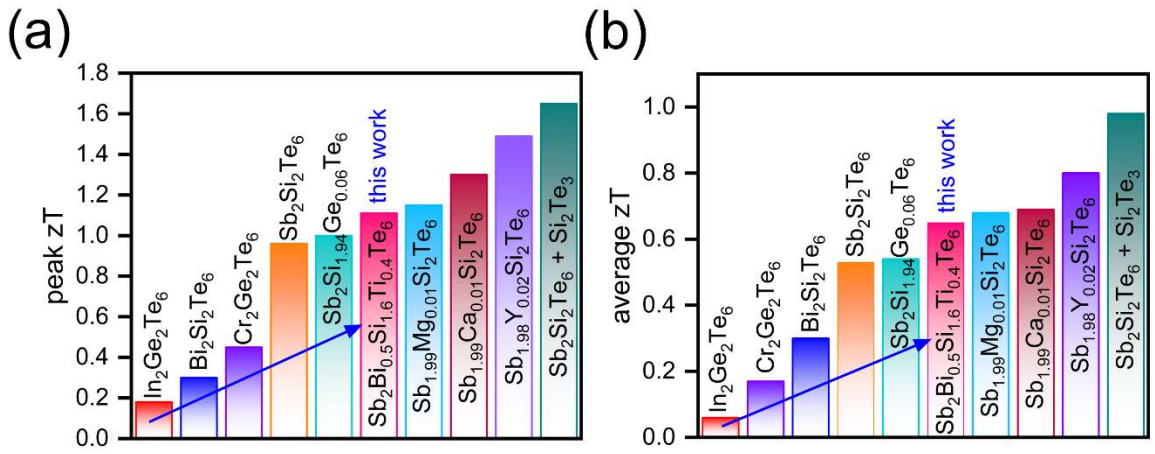

Figure 1. (a) Peak zT, (b) average zT values of $Sb_2Si_2Te_6$-related materials reported in the literature. ($In_2Ge_2Te_6$,[28] $Bi_2Si_2Te_6$,[35] $Cr_2Ge_2Te_6$,[28] $Sb_2Si_2Te_6$,[8] $Sb_2Si_{1.94}Ge_{0.06}Te_6$,[36] $Sb_{1.5}Bi_{0.5}Ti_{0.3}Si_{1.6}Te_6$ (this work), $Sb_{1.99}Mg_{0.01}Si_2Te_6$,[37] $Sb_{1.99}Ca_{0.01}Si_2Te_6$,[38] $Sb_{1.98}Y_{0.02}Si_2Te_6$[39], ($Sb_2Si_2Te_6$ + Si_2Te_3).[8]

In the literature, Ti-doping has been widely applied to various thermoelectric materials to enhance their performance.[41, 42] In particular, Ti doping in $Yb_{0.4}Co_4Sb_{12}$,[43] $AgSbTe_2$[44] and $Bi_{0.5}Sb_{1.5}Te_6$[45] has been shown to increase carrier concentration, and reduce lattice thermal conductivity for $AgSbTe_2$ and $Bi_{0.5}Sb_{1.5}Te_6$. Additionally, Ti doping has improved band degeneracy in GeTe[46] and intriguingly, it has been observed to switch the p-type nature of SnSe to n-type.[47]

Pristine $Sb_2Si_2Te_6$ exhibits an optimized[4] carrier concentration around $8x10^{19}$ cm^{-3}, and electrical/thermal conductivity values comparable to state of art thermoelectric materials such as BiSbTe[48] and GeTe[41], respectively. However, the Seebeck coefficient of $Sb_2Si_2Te_6$ is low compared to optimum values corresponding to its thermal conductivity between 0.4 - 1.5 $Wm^{-1}K^{-1}$.[49] As a result, the thermoelectric performance of $Sb_2Si_2Te_6$ can be increased for sustainable and clean energy solutions.

In this study, we present a high entropy alloying strategy for $Sb_2Si_2Te_6$ by co-alloying with Bi and Ti, optimizing the Seebeck coefficient in the range of 202 – 230 μVK^{-1}. High-entropy

engineering has been widely applied in thermoelectric materials such as $AgMnGePbSbTe_5$[50], PbSe[51], GeTe[52], and $AgBiPbSe_2S$[53] to enhance both thermoelectric and mechanical performance. The high-symmetry lattice observed in these materials contribute to excellent electrical properties, while short-range disorder induces lattice distortions and phonon delocalization.[54] Additionally, careful tuning of composition increases local chemical fluctuation and effectively reduces the lattice thermal conductivity.[55] Bi alloying in $Sb_2Si_2Te_6$ effectively reduces lattice thermal conductivity while preserving crystal symmetry, and Ti alloying helps maintain electrical conductivity. Debye – Callaway model indicates that the reduction in lattice thermal conductivity in $Sb_{1.5}Bi_{0.5}Si_{1.6}Ti_{0.3}Te_6$ is primarily due to enhanced point defect scattering. Consequently, the quality factor is increased, contributing to a zT of 1.11 at 673 K. The performance of $Sb_{1.5}Bi_{0.5}Si_{1.6}Ti_{0.3}Te_6$ surpasses that of most 2D-related materials, and SPB model suggests that its performance could be further leveraged to 1.2 by fine-tuning the Fermi level. Therefore, this study demonstrates a promising high-entropy alloying strategy for optimizing the performance of thermoelectric materials.

2. Methodology

The nominal compositions of $Sb_{1.5}Bi_{0.5}Si_xTi_yTe_6$ (including $Sb_2Si_2Te_6$, $Sb_{1.5}Bi_{0.5}Si_2Te_6$, $Sb_{1.5}Bi_{0.5}Si_{1.8}Ti_{0.2}Te_6$, $Sb_{1.5}Bi_{0.5}Si_{1.6}Ti_{0.3}Te_6$, $Sb_{1.5}Bi_{0.5}Si_{1.6}Ti_{0.3}Te_6$) were prepared by weighing pure elements inside an Ar-filled glovebox. The elements were loaded into stainless steel jars (50 mL) with 4 stainless steel balls (10 mm diameter) under an inert Argon atmosphere. Afterwards, the mixture was pulverized using high-energy ball milling (SPEX 8000D), at a speed of 1725 rpm for 90 minutes. After milling, the resulting powders were loaded into quartz ampoules and vacuum sealed before the heat treatment at 823 K for 48 hours. The resulting ingots were sintered by Spark Plasma Sintering (SPS, Ed-PassIVJ, 6T-3P-30, Japan) by heating to 773 K over 10 minutes, followed by annealing for 5 minutes under a pressure of 60 MPa. Due to the anisotropic nature of $Sb_2Si_2Te_6$, the samples were cut into in-plane and cross-plane orientations. The representation of cutting direction is provided in Figure 4(a).

The electrical and thermal transport properties of samples were measured through cross-plane direction, which is parallel to the pressing direction. Electrical resistivity and Seebeck coefficient were measured using a ZEM – 3 system. The thermal diffusivity was determined using the Laser Flash Analysis (LFA) technique with a NETZSCH instrument. Thermal conductivity was calculated using the following equation: $\kappa = D \times C_p \times \rho$ where D, C_p, and ρ represent diffusivity, specific heat capacity, and geometrical density, respectively. The heat

capacity values of $Sb_2Si_2Te_6$ were obtained from the literature.[8] Thermogravimetric analysis of samples were done using TA instruments SDT Q600 TGA. The Hall effect measurement with Van der Pauw method was used to measure charge carrier concentration (n_H) and the carrier mobility (μ_H), utilizing a Bio-Rad Microscience, Hall measurement system, HL5500 (United States).

The crystalline phases in the samples were identified using X-ray diffraction (XRD) analysis with a Bruker D8 Advance diffractometer and Cu K_α radiation. The step size was 0.02°, and the 2θ range was 10° to 80°. Microstructural and elemental analyses were carried out using a field-emission scanning electron microscope (FESEM, JEOL JSM 7600F) containing an energy-dispersive X-ray spectrometer (EDS) detector. The nanostructure and morphologies were identified by a Transmission electron microscope (TEM, JEOL JEM-2100F, Japan). The error limits for electrical conductivity, Seebeck coefficient, thermal conductivity, power factor, and zT were assumed to be 5%, 3%, 7%, 7% and 10%, respectively.[40, 56-58] A detailed explanation for the error limits is also provided in supporting information.

3. Results and Discussion

The phase structures of $Sb_2Si_2Te_6$, $Sb_{1.5}Bi_{0.5}Si_2Te_6$, $Sb_{1.5}Bi_{0.5}Si_{1.7}Ti_{0.3}Te_6$, $Sb_{1.5}Bi_{0.5}Si_{1.6}Ti_{0.3}Te_6$, $Sb_{1.5}Bi_{0.5}Si_{1.8}Ti_{0.2}Te_6$ were identified using X-ray diffraction, as shown in Figure 2(a). As a reference, the .cif file and intensity vs. 2θ values of $Sb_2Si_2Te_6$ (CDCC#1947640) were obtained from the literature.[8] Maintaining structural integrity during high entropy alloying is crucial. The pristine $Sb_2Si_2Te_6$ and Bi alloyed $Sb_{1.5}Bi_{0.5}Si_2Te_6$ are indexed to space group of $R\bar{3}$. However, Ti alloyed samples show additional phases of $TiTe_2$, Sb_2Te_3 and Si_2Te_3, suggesting the decomposition of $Sb_2Si_2Te_6$. $Sb_2Si_2Te_6$ is known to decompose into Sb_2Te_3 and Si_2Te_3, particularly at high temperatures and high doping levels.[36, 38, 39] Thermogravimetric analyses (TGA,Figure S1) of all samples reveal that the samples undergo a slight decomposition (less than 0.8% in weight), and the decomposition increases with Bi/Ti co-alloying. A detailed explanation on the decomposition and TGA analysis is reported in the supporting information. Observed secondary phases in the best-performing $Sb_{1.5}Bi_{0.5}Si_{1.6}Ti_{0.3}Te_6$ can contribute to its ultralow thermal conductivity, which will be explained in the following sections.

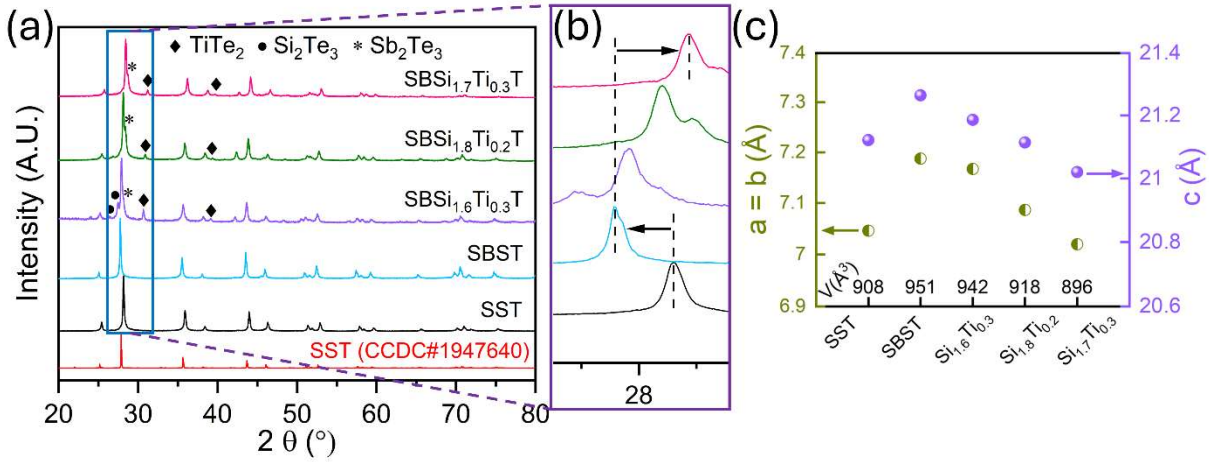

Figure 2. Powder XRD (a) between 2θ=20 – 80°, (b) zoomed in diffractogram between 2θ = 27 – 29°, (c) lattice parameters of $Sb_2Si_2Te_6$, $Sb_{1.5}Bi_{0.5}Si_2Te_6$, $Sb_{1.5}Bi_{0.5}Si_{1.7}Ti_{0.3}Te_6$, $Sb_{1.5}Bi_{0.5}Si_{1.6}Ti_{0.3}Te_6$, $Sb_{1.5}Bi_{0.5}Si_{1.8}Ti_{0.2}Te_6$

Figure 2(b) depicts a zoomed-in XRD diffractogram of all samples, which reveal changes in the lattice parameters with Bi and Ti alloying. Since Bi^{3+} has a larger ionic radius than Sb^{3+}, the replacement of Bi enlarges the lattice, which is observed as a shift to the left in the XRD shown in Figure 2(b). This trend is consistent with the literature: for instance, Chen et al. reported a decrease in lattice parameters when Sb substitutes Bi in $Bi_2Si_2Te_6$,[35] and it is well established that $Bi_2Si_2Te_6$ has larger lattice parameters than $Sb_2Si_2Te_6$. [34] In our case, we substitute Bi into $Sb_2Si_2Te_6$, which supports the observed lattice expansion. On the other hand, Ti^{4+} has a smaller radius than Si^{4+}. Therefore, replacement of Si with Ti shrinks the lattice, as shown by Rietveld refinement results depicted in Figure 2(c). These results are in accordance with the literature[36, 45] and Vegard's law.

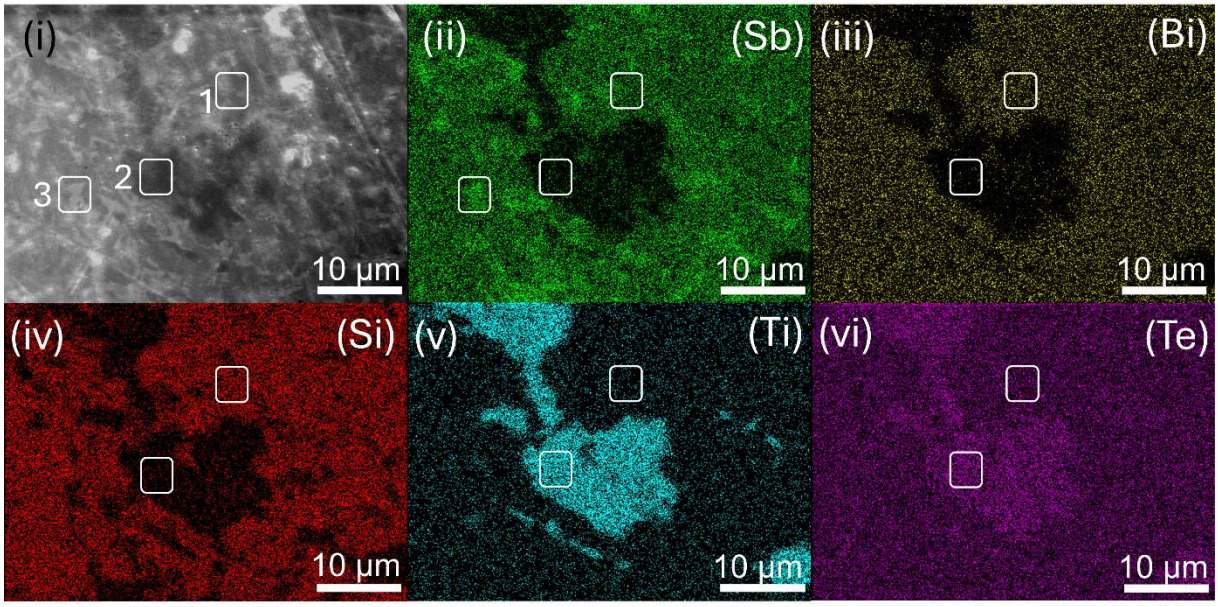

Figure 3. Microstructural characterization of $Sb_{1.5}Bi_{0.5}Si_{1.6}Ti_{0.3}Te_6$, (a) SEM image, elemental maps showing the distribution of (ii) Sb, (iii) Bi, (iv) Si, (v) Ti, and (vi) Te.

To further elucidate the identity of precipitates, microstructural characterization of pristine $Sb_2Si_2Te_6$ and $Sb_{1.5}Bi_{0.5}Si_{1.6}Ti_{0.3}Te_6$ was performed using Scanning Electron Microscopy (SEM) and Energy Dispersive X-Ray Spectroscopy (EDS). As shown in Figure 3, the sample exhibits three distinct regions, and atomic percent of each element is provided in Table 1. EDS studies (Figure S2) on $Sb_2Si_2Te_6$ reveal nearly homogenous distribution of Sb, Si and Te along with slight Sb vacancies, in alignment with the literature.[8] On the SEM image of $Sb_{1.5}Bi_{0.5}Si_{1.6}Ti_{0.3}Te_6$ (Figure 3), the first three regions are highlighted by white boxes, while a fourth region represents the overall matrix. Region 1, as indicated by the elemental mapping images in Figure 3(ii, iii, iv, v, and vi), contains all elements except Ti. EDS analysis of this region reveals a composition of $Sb_{0.69}Bi_{0.29}Si_{1.04}Te_3$. Region 2 shows clear precipitates of $TiTe_2$, as evidenced by Ti and Te in the elemental maps (Figure 3(v) and (vi)) and the corresponding EDS results (Table 1). Region 3 is characterized by an excess of Sb and a deficiency of Si, with a reported composition of $Bi_{0.35}Sb_{1.65}Te_3$. These observations indicate the presence of impurity phases such as $TiTe_2$, $(Bi,Sb)_2Si_2Te_3$, and $(Bi,Sb)_2Te_3$. Since $(Bi,Sb)_2Si_2Te_3$ and $(Bi,Sb)_2Te_3$ cannot be detected in XRD, it can be concluded that their amount is quite low. The significant lattice parameter mismatch between $Sb_2Si_2Te_6$ (a=7.167, c=21.186[8]) and $TiTe_2$ (a=3.78, c=6.50[59]) may contribute to the reduced lattice thermal conductivity observed in $Sb_{1.5}Bi_{0.5}Si_{1.6}Ti_{0.3}Te_6$.

Table 1 Detailed quantification results revealing the atomic percent of each element of $Sb_{1.5}Bi_{0.5}Si_{1.6}Ti_{0.3}Te_6$, with regions shown in Figure 3.

Region	Sb (%)	Bi (%)	Si (%)	Ti (%)	Te (%)
1	13.93	5.70	20.48	-	59.90
2	-	-	3.50	29.34	67.15
3	33.28	6.94	-	-	59.77

The thermoelectric transport properties of $Sb_2Si_2Te_6$ (SST), $Sb_{1.5}Bi_{0.5}Si_2Te_6$ (SBST), $Sb_{1.5}Bi_{0.5}Si_{1.8}Ti_{0.2}Te_6$, $Sb_{1.5}Bi_{0.5}Si_{1.6}Ti_{0.3}Te_6$, and $Sb_{1.5}Bi_{0.5}Si_{1.7}Ti_{0.3}Te_6$ are reported in Figure 4. Given the anisotropic nature of $Sb_2Si_2Te_6$, all measurements were collected along the cross-plane direction, which is parallel to the pressing direction of the SPS process. The cutting scheme is reported in Figure 4(a). As shown in Figure 4(b), the electrical conductivity of pristine $Sb_2Si_2Te_6$ (SST) and $Sb_{1.5}Bi_{0.5}Sb_2Te_6$ decreases with increasing temperature, indicating degenerate semiconducting behavior. Bi alloying significantly lowers the electrical conductivity of SST, which can be attributed to the approximately tenfold lower carrier concentration in $Bi_2Si_2Te_6$ compared to $Sb_2Si_2Te_6$ [34]. Further reduction in electrical conductivity is observed with Ti alloying in $Sb_{1.5}Bi_{0.5}Si_2Te_6$ due to reduced carrier concentration, as reported in Table 2. In addition, Bi/Ti co-alloyed samples exhibit non-degenerate semiconducting behavior due to reduced changed scattering mechanism and reduced carrier concentration. Among all Ti-alloyed samples, $Sb_{1.5}Bi_{0.5}Si_{1.6}Ti_{0.3}Te_6$ shows the highest electrical conductivity due to its higher carrier concentration as reported in (Table 2). A detailed explanation on the carrier concentration is provided in the next sections.

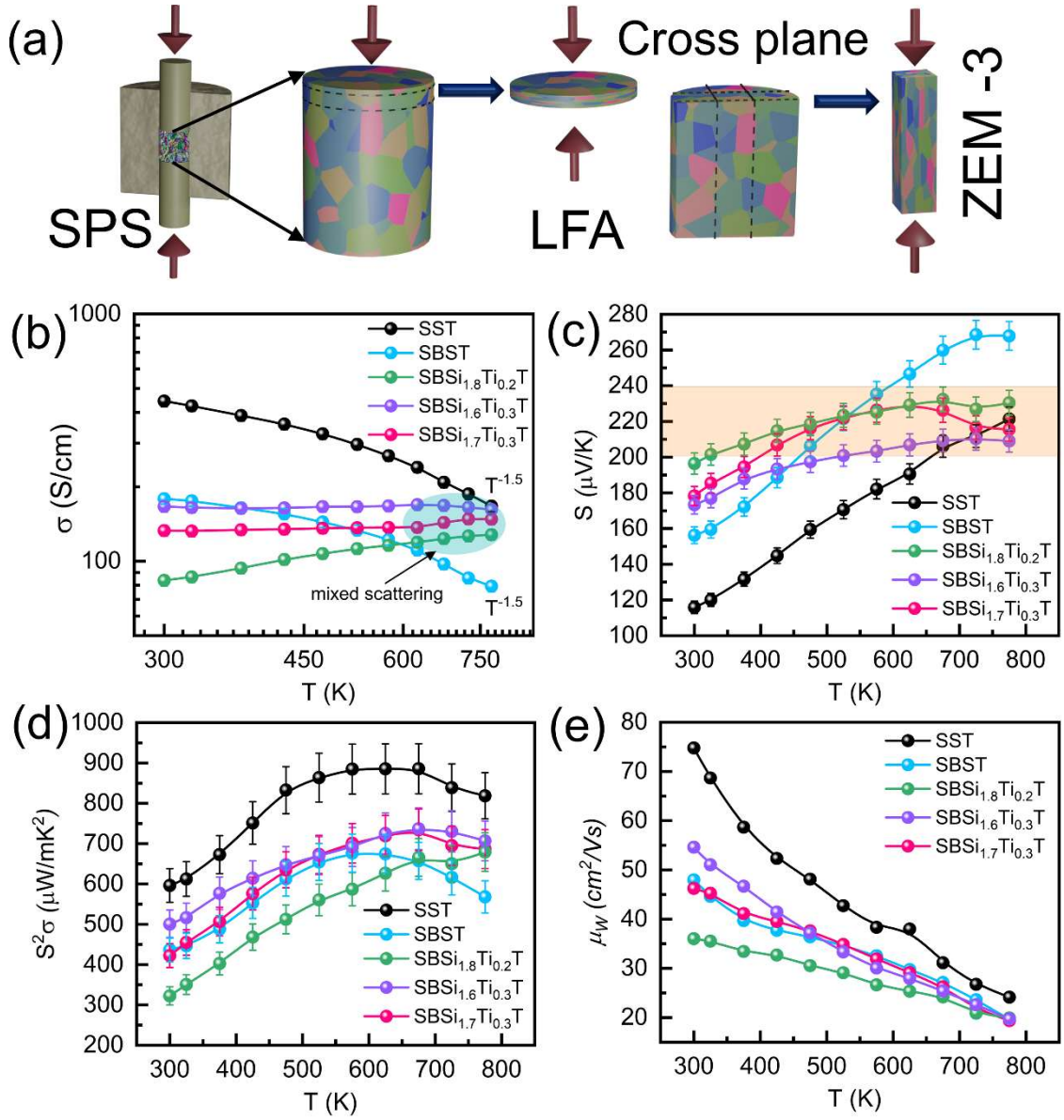

Figure 4. (a) Schematic showing how samples are cut after they are densified by SPS. Temperature-dependent (b) electrical conductivity, (c) Seebeck coefficient, (d) power factor, (e) weighted mobility of $Sb_2Si_2Te_6$, $Sb_{1.5}Bi_{0.5}Si_2Te_6$, $Sb_{1.5}Bi_{0.5}Si_{1.8}Ti_{0.2}Te_6$, $Sb_{1.5}Bi_{0.5}Si_{1.6}Ti_{0.3}Te_6$, $Sb_{1.5}Bi_{0.5}Si_{1.7}Ti_{0.3}Te_6$.

A combined evaluation of electrical conductivity and weighted mobility provides insights into the scattering mechanisms of the samples. $Sb_2Si_2Te_6$ and $Sb_{1.5}Bi_{0.5}Si_2Te_6$ exhibit a $T^{-1.5}$ relationship between electrical conductivity and temperature, indicative of acoustic phonon scattering. This indicates that acoustic phonon scattering dominates at high temperatures, reducing the electrical conductivity (σ, Figure 4(b)) and electronic thermal conductivity (κ_e, Figure 5(b)). In contrast, the Bi-Ti alloyed samples (circled by green in Figure 4(b)) display a mixed scattering mechanism. These samples show lower electrical conductivity compared to

$Sb_2Si_2Te_6$ and $Sb_{1.5}Bi_{0.5}Si_2Te_6$, indicating that alloy scattering plays a significant role. Consequently, the electrical conductivity and mobilities of the Bi/Ti co-alloyed samples are reduced. This shift in the scattering mechanism, which has also been observed in Mg_3Sb_2[60], results in decreased Hall mobility and weighted mobility as the scattering transitions from acoustic to mixed types.[61] A more detailed discussion on mobilities is provided in the following sections.

As reported in Figure 4(c), the Seebeck coefficients of all samples exhibit positive values, confirming their p-type conduction behavior. For $Sb_2Si_2Te_6$, the Seebeck coefficient increases with temperature, suggesting a large bandgap and degenerate semiconducting nature. However, the Seebeck coefficient of Bi alloyed $Sb_{1.5}Bi_{0.5}Si_2Te_6$ reaches a plateau at 700 K, similar to $Bi_2Si_2Te_6$ showing a downturn of the Seebeck coefficient at high temperatures. Additionally, the room-temperature Seebeck coefficient of $Sb_{1.5}Bi_{0.5}Si_2Te_6$ is higher than that of $Sb_2Si_2Te_6$, consistent with its lower carrier concentration. As shown in Table 2, Bi-alloyed $Sb_{1.5}Bi_{0.5}Si_2Te_6$ exhibits a lower carrier concentration and higher effective mass compared to $Sb_2Si_2Te_6$, which accounts for its enhanced Seebeck coefficient.

Ti-alloyed samples show a noticeable optimization of the Seebeck coefficient, ranging between 202 - 230 μVK^{-1}, with the corresponding lattice thermal conductivity spanning from 0.4 – 1.5 $Wm^{-1}K^{-1}$ [49]. The enhancement in Seebeck coefficient in Bi/Ti co-alloyed samples, especially $Sb_{1.5}Bi_{0.5}Si_{1.6}Ti_{0.3}Te_6$, stems from the reduced carrier concentration and significantly enhanced effective mass, as reported in Table 2. The power factor of Bi/Ti co-alloyed $Sb_2Si_2Te_6$ samples are reported in Figure 4 (d). Although the power factor values of all alloyed samples are lower than that of pristine $Sb_2Si_2Te_6$, $Sb_{1.5}Bi_{0.5}Si_{1.6}Ti_{0.3}Te_6$ demonstrates the highest power factor among all Bi/Ti co-alloyed samples.

To understand the overall impact on Bi/Ti co-alloying, we analyzed the carrier concentration and Hall mobility through the Single Parabolic Band (SPB) model. Pisarenko plot, as shown in Figure 5(a), establishes the relationship between Seebeck coefficient and Hall carrier concentration. The density of states effective mass (m^*) of pure $Sb_2Si_2Te_6$ is 1.15 m_e, whereas $Sb_{1.5}Si_{0.5}Si_{1.6}Ti_{0.3}Te_6$ exhibits an increased m^* of 1.9 m_e due to co-alloying with Bi and Ti. In addition, replacement of Sb with Bi and Si with Ti results in increased m^* in all samples due to higher atomic masses of Bi/Ti compared to Sb/Si.

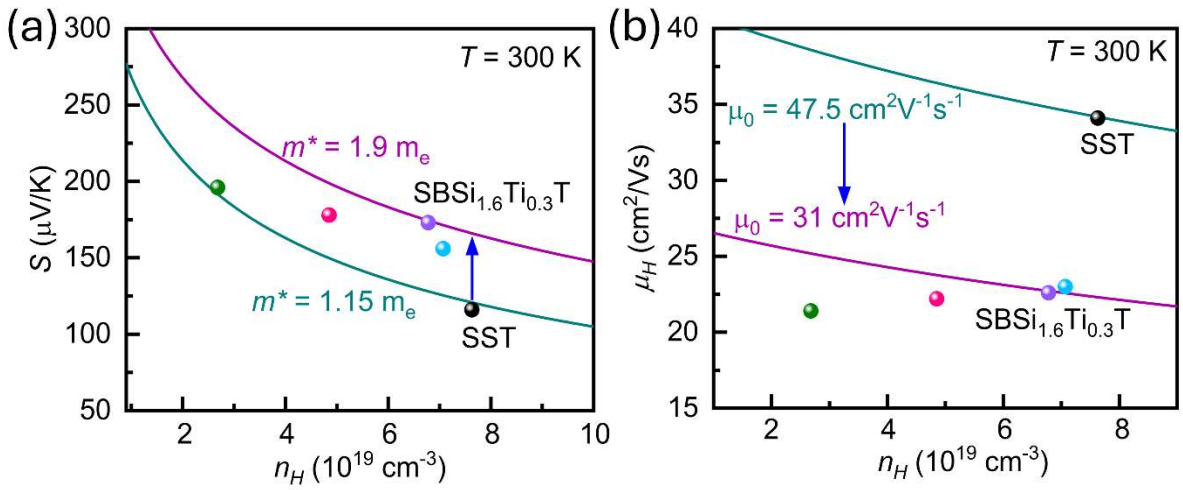

Figure 5. (a) Pisarenko plot showing the relationship between Seebeck coefficient and the carrier concentration at 300 K. (b) Hall mobility versus carrier concentration, revealing the drift mobility (μ_0), at 300 K.

Figure 5(b) reveals that the drift mobility (μ_0) of $Sb_{1.5}Bi_{0.5}Si_{1.6}Ti_{0.3}Te_6$ can be fitted to 31 $cm^2V^{-1}S^{-1}$, which is less than that that of pristine $Sb_2Si_2Te_6$ (47.5 $cm^2V^{-1}s^{-1}$). In addition, all Bi-Ti alloyed samples exhibit reduced drift mobilities (μ_0) compared to pristine $Sb_2Si_2Te_6$. This reduction is consistent with the observed decreases in Hall mobilities and (μ_H) and electrical conductivities (σ) in the alloyed samples, suggesting a transition in the dominant carrier scattering mechanism from acoustic to mixed scattering.

Table 2 Electrical transport properties of $Sb_2Si_2Te_6$, $Sb_{1.5}Bi_{0.5}Si_{1.6}Ti_{0.3}Te_6$, $Sb_{1.5}Bi_{0.5}Si_{1.6}Ti_{0.3}Te_6$, $Sb_{1.5}Bi_{0.5}Si_{1.7}Ti_{0.3}Te_6$, and $Sb_{1.5}Bi_{0.5}Si_{1.8}Ti_{0.3}Te_6$ at 300 K.

Composition	n_H ($10^{19}cm^{-3}$)	S (μVK^{-1})	m^* (m_e)	σ (Scm^{-1})	μ_W ($cm^2V^{-1}s^{-1}$)	μ_H ($cm^2V^{-1}s^{-1}$)
$Sb_2Si_2Te_6$	7.63	116	1.15	444.3	74.8	34.1
$Sb_{1.5}Bi_{0.5}Si_2Te_6$	7.07	156	1.65	178.9	48.0	23.0
$Sb_{1.5}Bi_{0.5}Si_{1.6}Ti_{0.3}Te_6$	6.78	173	1.90	166.5	54.6	22.6
$Sb_{1.5}Bi_{0.5}Si_{1.7}Ti_{0.3}Te_6$	4.85	178	1.55	132.8	46.2	22.2
$Sb_{1.5}Bi_{0.5}Si_{1.8}Ti_{0.2}Te_6$	2.68	196	1.25	83.5	36.0	21.4

Room temperature (300 K) carrier concentration (n_H), Seebeck coefficient (S), density of states effective mass (m^*), electrical conductivity (σ), weighted (μ_W) and Hall mobilities (μ_H) of all samples are reported in Table 2. The carrier concentration of pristine $Sb_2Si_2Te_6$ is $7.63x10^{19}$ cm^{-3}, which is in accordance with the results in literature.[8] The carrier concentration drops to $7.07x10^{19}$ cm^{-3} with Bi doping in the $Sb_{1.5}Bi_{0.5}Si_2Te_6$. This could be ascribed to possible

formation of n-type Te_{Bi} antisite defects instead of p-type Sb_{Te} defects which are responsible of the p-type conduction in $Sb_2Si_2Te_6$. [34] The carrier concentration further drops to $6.78x10^{19}$ cm^{-3} in $Sb_{1.5}Bi_{0.5}Si_{1.6}Ti_{0.3}Te_6$ by replacing 0.4 Si atoms with 0.3 Ti atoms and intentionally adding V^{2-}_{Si} vacancies. For $Sb_{1.5}Bi_{0.5}Si_{1.8}Ti_{0.2}Te_6$ and $Sb_{1.5}Bi_{0.5}Si_{1.7}Ti_{0.3}Te_6$ the drop in carrier concentration can be explained by electron counting. For instance, $Sb_2Si_2Te_6$ has 3(Si) x 2 = 6, whereas $Sb_{1.5}Bi_{0.5}Si_{1.8}Ti_{0.2}Te_6$ has 3(Si) x 1.8 + 4(Ti) x 0.2 = 6.2 electrons, which reduce the carrier concentration. As a result of the reduced carrier concentration, the Seebeck coefficient of Bi/Ti co-alloyed samples increases. The Seebeck coefficient in semiconductors depends on the Fermi level and the band edge.[62] In p-type semiconductors like $Sb_2Si_2Te_6$, a reduction in carrier concentration shifts Fermi level away from the valence band, leading to an increase in Seebeck coefficient.[4] Additionally, Bi-Ti alloyed samples exhibit decreased Hall (μ_H) and weighted (μ_W) mobilities compared to pristine $Sb_2Si_2Te_6$, confirming the transition of the dominant carrier scattering mechanism from acoustic to mixed. A similar phenomenon was observed by Shuai et. al for $Mg_{3.2}Sb_{1.5}Bi_{0.5}$. [60]

In order to elaborate the effect of Bi/Ti co- alloying independent from the alterations in carrier concentration, we calculated the weighted mobility of the samples and reported in Figure 4(e). Since electrons scatter phonons, all samples display decreasing weighted mobilities with increasing temperature. In literature, the weighted mobility of Bi alloyed samples is lower than pristine $Sb_2Si_2Te_6$, likely due to the inherent resistance of $Sb_2Si_2Te_6$ to carrier scattering at grain boundaries. As a result, the weighted mobility of $Sb_2Si_2Te_6$ is higher than that of $Bi_2Si_2Te_6$[34] which supports the reduced weighted mobility of $Sb_{1.5}Bi_{0.5}Si_2Te_6$, $Sb_{1.5}Bi_{0.5}Si_{1.6}Ti_{0.3}Te_6$, $Sb_{1.5}Bi_{0.5}Si_{1.7}Ti_{0.3}Te_6$, and $Sb_{1.5}Bi_{0.5}Si_{1.8}Ti_{0.2}Te_6$ compared to $Sb_2Si_2Te_6$. Pristine $Sb_2Si_2Te_6$ and Bi-alloyed $Sb_{1.5}Bi_{0.5}Si_2Te_6$ exhibit a $T^{-1.5}$ relationship between weighted mobility and temperature, indicative of electron-phonon scattering.[34] However, for $Sb_{1.5}Bi_{0.5}Si_{1.6}Ti_{0.3}Te_6$, $Sb_{1.5}Bi_{0.5}Si_{1.8}Ti_{0.2}Te_6$, $Sb_{1.5}Bi_{0.5}Si_{1.7}Ti_{0.3}Te_6$, this $T^{-1.5}$ relationship is disrupted, suggesting that the scattering behavior is altered by Bi/Ti co-alloying. The reduced weighted mobility values indicate that the band structure is also affected by Bi and Ti alloying. This decrease in weighted mobility correlates with a reduced power factor in all samples. Despite the lower power factor,

the thermoelectric figure of merit (zT) of $Sb_{1.5}Bi_{0.5}Si_{1.6}Ti_{0.3}Te_6$ increases. To explain this, we evaluated the thermal conductivity of all samples, which is reported in Figure 6.

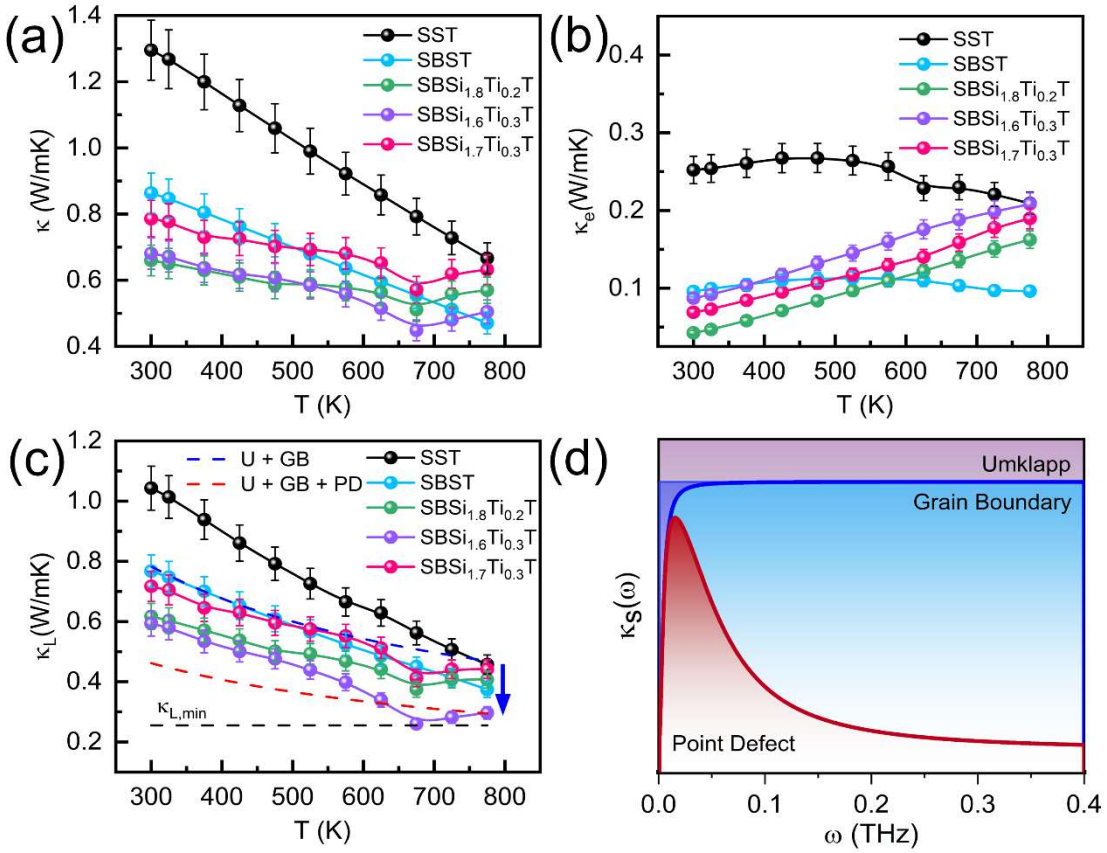

Figure 6. Temperature-dependent (a) total, (b) electronic, (c) lattice thermal conductivity of $Sb_2Si_2Te_6$, $Sb_{1.5}Bi_{0.5}Si_2Te_6$, $Sb_{1.5}Bi_{0.5}Si_{1.8}Ti_{0.2}Te_6$, $Sb_{1.5}Bi_{0.5}Si_{1.6}Ti_{0.3}Te_6$, $Sb_{1.5}Bi_{0.5}Si_{1.7}Ti_{0.3}Te_6$. (d) Debye Callaway model of lattice thermal conductivity of $Sb_{1.5}Bi_{0.5}Si_{1.6}Ti_{0.3}Te_6$.

Figure 6(a) reveals that the total thermal conductivities Bi/Ti co-alloyed samples are lower than that of pristine $Sb_2Si_2Te_6$. In solids, the heat is carried by both electrons and phonons, so electronic and lattice thermal conductivities of all samples are shown in Figure 6(b) and Figure 6(c), respectively. The electronic thermal conductivities of samples were calculated through Wiedemann Franz law, $\kappa_e = L.\sigma.T$ where L is the Lorenz number calculated by Single Parabolic Band Model. (Details are provided in Supporting Information). The electronic thermal conductivities of all samples follow the same trend as electrical conductivity due to the direct relationship between these properties.

As shown in Figure 6(c), the lattice thermal conductivities of $Sb_2Si_2Te_6$ and $Sb_{1.5}Bi_{0.5}Si_2Te_6$ decrease with increasing temperature, consistent with their sufficiently large bandgaps. However, for Ti-alloyed samples $Sb_{1.5}Bi_{0.5}Si_{1.8}Ti_{0.2}Te_6$, $Sb_{1.5}Bi_{0.5}Si_{1.6}Ti_{0.3}Te_6$,

$Sb_{1.5}Bi_{0.5}Si_{1.7}Ti_{0.3}Te_6$, the lattice thermal conductivity decreases up to 673 K and then begins to increase at higher temperatures. This upturn suggests the onset of bipolar conduction, where the activation of opposite charge carriers contributes to heat transport, likely due to a reduction in the bandgap induced by alloying. For Bi/Ti co-alloyed samples, reduced carrier concentration supports the possibility of increased bipolar conduction. Additionally, all Bi/Ti co-alloyed samples exhibit lower lattice thermal conductivities than pristine $Sb_2Si_2Te_6$, likely due to the phonon scattering centers induced by alloying. $TiTe_2$ is a possible contributor to this effect.

To comprehensively analyze the thermal conductivity, we modelled the thermal conductivities at the onset of bipolar conduction, focusing on Umklapp, grain boundary, and point defect scattering within the Debye – Callaway model, and reported in Figure 6(d). Point defects are well known to scatter phonons at low – to – medium frequencies, significantly impacting thermal transport.[14, 63] Similarly in this study, point defects are the main sources of phonon scattering at low frequency and low lattice thermal conductivity of $Sb_{1.5}Bi_{0.5}Si_{1.6}Ti_{0.3}Te_6$. As shown in Figure 6(c) and Figure 6(d), point defect scattering effectively lowers the lattice thermal conductivity to values approaching the amorphous limit. In addition, Bi/Ti co-alloying increases lattice distortion, which further reduces the lattice thermal conductivity by enhancing phonon scattering. The presence of these distortions disrupts the periodicity of the crystal lattice, leading to increased phonon-phonon interactions and phonon scattering at low and high frequencies. Similar phenomena have been observed in other high-entropy systems, where alloying-induced lattice distortions significantly impact thermal transport.[15, 64]

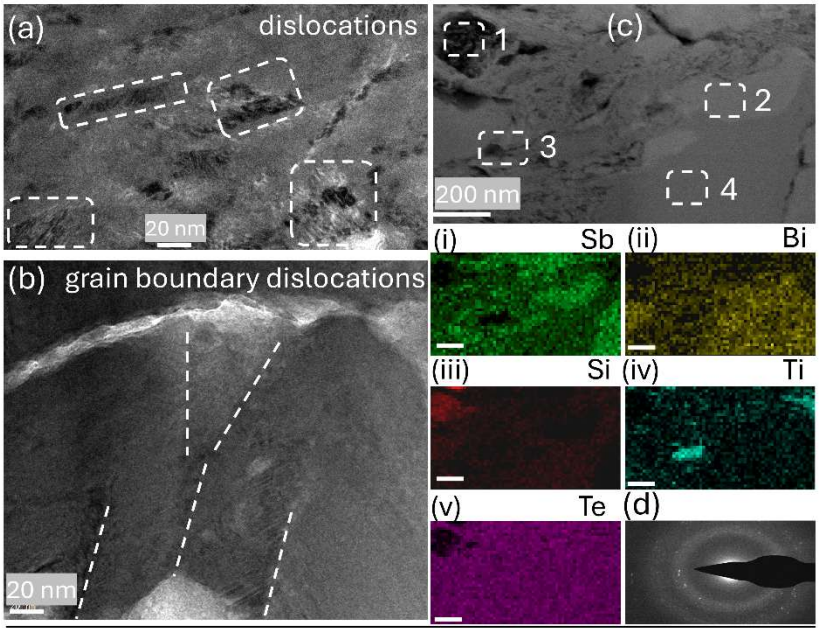

(e) Region	Sb (%)	Bi (%)	Si (%)	Ti (%)	Te (%)
1	10.19	1.29	55.72	2.03	57.41
2	33.28	1.07	10.32	3.46	51.87
3	1.70	0.14	5.14	49.56	43.45
4	26.58	0.17	23.54	4.25	45.46

Figure 7. HRTEM image of $Sb_{1.5}Bi_{0.5}Si_{1.6}Ti_{0.3}Te_6$ showing (a) high-density dislocations, (b) grain boundaries, (c) elemental distributions of (i) Sb, (ii) Bi, (iii) Si, (iv) Ti, and (v) Te. (d) SAED image of $Sb_{1.5}Bi_{0.5}Si_{1.6}Ti_{0.3}Te_6$. (e) Detailed quantification results revealing the atomic percentage of each element.

In order to evaluate the reduction in lattice thermal conductivity, we examined $Sb_{1.5}Bi_{0.5}Si_{1.6}Ti_{0.3}Te_6$ through High-Resolution Transmission Electron Microscopy (HRTEM), as shown in Figure 7. Figure 7 (a) and Figure 7 (b) reveal a high density of dislocations and grain boundaries, both of which contribute to the reduction of lattice thermal conductivity. Furthermore, the elemental maps presented in Figures 7(c), (i) – (v) clearly highlight the presence of Ti, Si, and Sb precipitates. The corresponding quantification data in Figure 7(e) further support the identification of these precipitates. Collectively, the presence of dislocations, grain boundaries, and precipitates significantly reduces the lattice thermal conductivity of $Sb_{1.5}Bi_{0.5}Si_{1.6}Ti_{0.3}Te_6$.

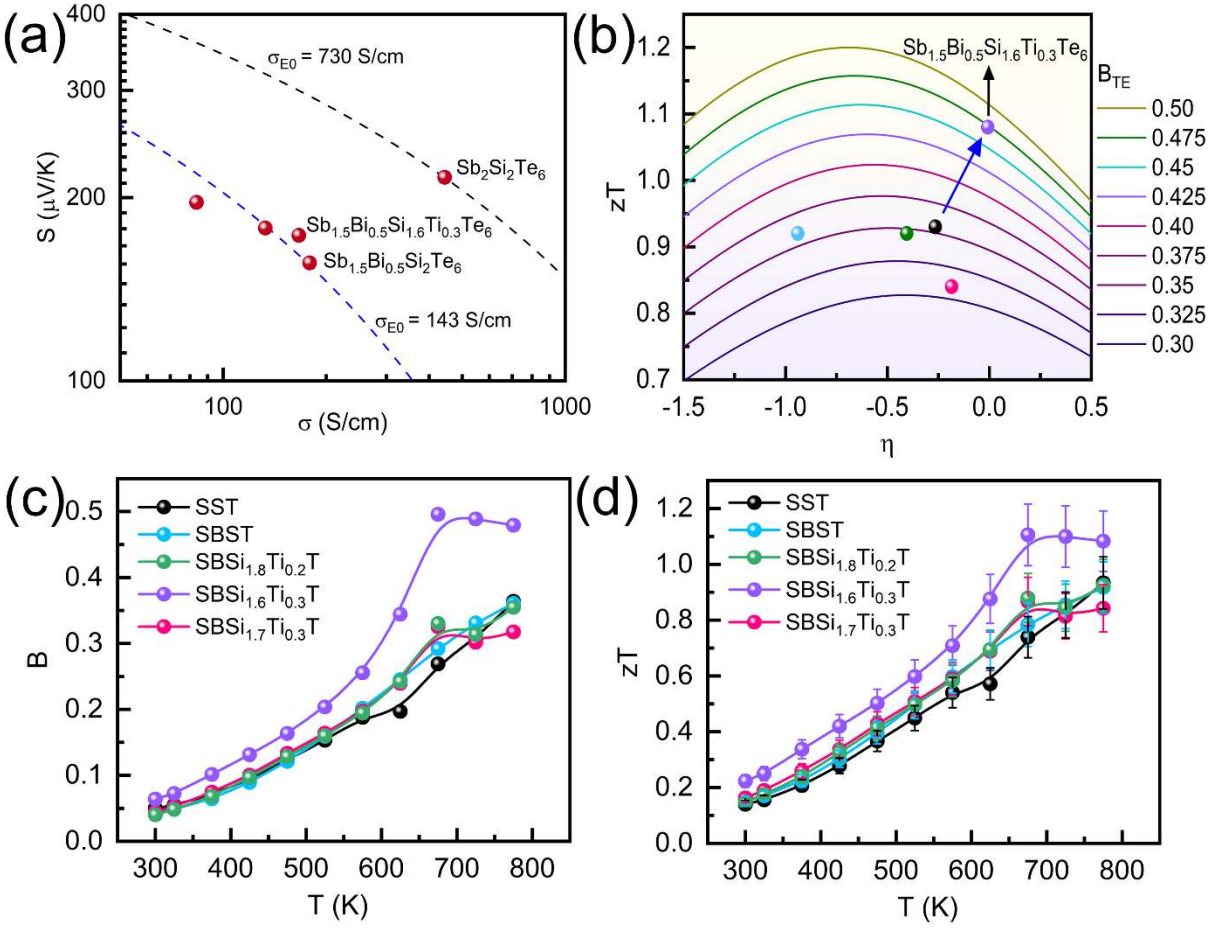

Figure 8. (a) Jonker plot, (b) Quality factor analysis based on the SPB model, temperature-dependent (b) quality factor, (b) zT of $Sb_2Si_2Te_6$, $Sb_{1.5}Bi_{0.5}Si_2Te_6$, $Sb_{1.5}Bi_{0.5}Si_{1.8}Ti_{0.2}Te_6$, $Sb_{1.5}Bi_{0.5}Si_{1.6}Ti_{0.3}Te_6$, $Sb_{1.5}Bi_{0.5}Si_{1.7}Ti_{0.3}Te_6$.

The quality factor ($B = \left(\frac{\kappa_B}{e}\right)^2 \frac{\sigma_{E_0}}{\kappa_L} T$) [65] is a good indicator of electronic properties independent of carrier concentration. At a specified temperature, it can be simplified as the ratio of electronic transport coefficient (σ_{E_0}) to lattice thermal conductivity. Electronic transport coefficient is a measure of electrical conductivity for an ideal material, without impurities or defects. Figure 8 (a) reveals that intrinsic electronic properties of $Sb_2Si_2Te_6$ deteriorates with Bi alloying. However, $Sb_{1.5}Bi_{0.5}Si_{1.6}Ti_{0.3}Te_6$ reveals the highest value among all Bi/Ti co-alloyed samples. Combined with its reduced lattice thermal conductivity, $Sb_2Bi_{0.5}Si_{1.6}Te_{0.3}$ results in the highest quality factor plateau of 0.48 between 675-775 K (Figure 8(c).). Hence, it can be concluded that Bi/Ti co-alloying improved the performance of $Sb_2Si_2Te_6$ in an ideally pure composition of $Sb_{1.5}Bi_{0.5}Si_{1.6}Ti_{0.3}Te_6$.

Since the thermoelectric performance of materials depends on their Fermi level, a comprehensive analysis using the single parabolic band (SPB) model[33] is crucial as shown in Figure 8(b). $Sb_{1.5}Bi_{0.5}Si_2Te_6$ exhibits a lower Fermi level compared to $Sb_2Si_2Te_6$, accounting for its reduced mobility. With Ti alloying, the Fermi level shifts upward, resulting in higher mobility for $Sb_{1.5}Bi_{0.5}Si_{1.6}Ti_{0.3}Te_6$ compared to $Sb_{1.5}Bi_{0.5}Si_2Te_6$. However, the primary improvement in quality factor stems from the reduction in lattice thermal conductivity. Consequently, $Sb_{1.5}Bi_{0.5}Si_{1.6}Ti_{0.3}Te_6$ has the potential to achieve a zT of 1.2 with the further optimization of the Fermi level.

The thermoelectric figure of merit (zT) of all samples is presented in Figure 8(d). Consistent with the trend observed in the quality factor, the zT values of all alloyed samples are higher than that of pristine $Sb_2Si_2Te_6$. Among them, $Sb_{1.5}Bi_{0.5}Si_{1.6}Ti_{0.3}Te_6$ exhibits the highest zT, primarily due to its significantly reduced lattice thermal conductivity. Figure 1 (a) and (b) demonstrate that $Sb_{1.5}Bi_{0.5}Si_{1.6}Ti_{0.3}Te_6$ achieves notable performance in both peak and average zT compared to reported $A_2B_2Te_6$ materials. With an average zT of 0.68, it ensures optimal efficiency across a wide temperature range, highlighting the potential of $Sb_2Si_2Te_6$ for broader application possibilities.

3. Conclusion

In this study, we applied a high-entropy alloying strategy to $Sb_2Si_2Te_6$ by co-alloying it with Bi and Ti. XRD and SEM analyses confirmed that the Bi/Ti co-alloyed samples retained the crystal structure of $Sb_2Si_2Te_6$, alongside the presence of impurity phases such as $TiTe_2$. Bi alloying significantly reduced lattice thermal conductivity primarily due to increased alloy and point defect scattering. The carrier concentration of Bi-Ti co-alloyed samples decreased to optimized levels, resulting in an optimized the Seebeck coefficient of approximately 210 μV/K. Furthermore, Bi-Ti co-alloying effectively fine-tuned the Fermi level, maintaining the favorable electrical properties of $Sb_2Si_2Te_6$. Jonker plot analysis and Pisarenko plot revealed that while the reduction on the carrier concentration slightly decreased intrinsic electronic transport, it notably enhanced the effective mass. The reduction in lattice thermal conductivity led to a sharp increase in the quality factor of $Sb_{1.5}Bi_{0.5}Si_{1.6}Ti_{0.3}Te_6$, resulting in an enhanced zT of 1.11 at 673 K. Notably, $Sb_{1.5}Bi_{0.5}Si_{1.6}Ti_{0.3}Te_6$ maintained a plateau of approximately 1.10 across a wide temperature range from 623 K to 723 K, rather than exhibiting a peak at only high temperatures. The thermoelectric performance of this composition could be further

enhanced by fine-tuning the effective mass and Fermi level, highlighting the potential of high entropy alloying in optimizing thermoelectric materials.

Acknowledgements

Q. Yan acknowledges the financial support from MOE ACRF Tier 1 RG78/23 and MOE TIER MOE-T2EP50223-0003. K. Saglik acknowledges the support from A*STAR's SINGA scholarship. The authors would like to acknowledge the Facility for Analysis, Characterization, Testing and Simulation (FACTS), Nanyang Technological University (NTU), Singapore.

Received: ((will be filled in by the editorial staff))
Revised: ((will be filled in by the editorial staff))
Published online: ((will be filled in by the editorial staff))

TOC Figure

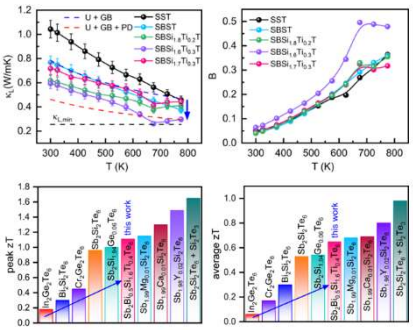

Bi and Ti co-alloying on $Sb_2Si_2Te_6$ effectively lowered lattice thermal conductivity while enhancing the quality factor. Additionally, improvements in electrical conductivity and the Seebeck coefficient led to a higher power factor. Consequently, the average *zT* and peak *zT* of $Sb_{1.5}Bi_{0.5}Si_{1.6}Ti_{0.3}Te_6$ significantly increased, surpassing other 2D materials reported in the literature.

ORCID IDs

Kivanc Saglik https://orcid.org/0000-0001-7910-8652
Jinfeng Dong https://orcid.org/0000-0002-3026-8054
Ady Suwardi https://orcid.org/0000-0002-7342-0431
Qingyu Yan https://orcid.org/0000-0003-0317-3225

References

[1] Li, J.-F.; Liu, W.-S.; Zhao, L.-D.; Zhou, M., *NPG Asia Mater.* **2010,** *2* (4), 152-158.
[2] Yan, Q.; Kanatzidis, M. G., *Nat. Mater.* **2022,** *21* (5), 503-513.
[3] Shakouri, A., *Annu. Rev. Mater. Res.* **2011,** *41* (1), 399-431.
[4] Snyder, G. J.; Toberer, E. S., *Nat. Mater.* **2008,** *7* (2), 105-114.
[5] Dong, J.; Jiang, Y.; Sun, Y.; Liu, J.; Pei, J.; Li, W.; Tan, X. Y.; Hu, L.; Jia, N.; Xu, B., *J. Am. Chem. Soc.* **2023,** *145* (3), 1988-1996.
[6] Zeier, W. G.; Zevalkink, A.; Gibbs, Z. M.; Hautier, G.; Kanatzidis, M. G.; Snyder, G. *J., Angew. Chem. Int. Ed.* **2016,** *55* (24), 6826-6841.
[7] Pecunia, V.; Silva, S. R. P.; Phillips, J. D.; Artegiani, E.; Romeo, A.; Shim, H.; Park, J.; Kim, J. H.; Yun, J. S.; Welch, G. C., *J. Phys. Mater.* **2023,** *6* (4), 042501.
[8] Luo, Y.; Cai, S.; Hao, S.; Pielnhofer, F.; Hadar, I.; Luo, Z.-Z.; Xu, J.; Wolverton, C.; Dravid, V. P.; Pfitzner, A.; Yan, Q.; Kanatzidis, M. G., *Joule* **2020,** *4* (1), 159-175. DOI https://doi.org/10.1016/j.joule.2019.10.010.
[9] Jia, N.; Cao, J.; Tan, X. Y.; Dong, J.; Liu, H.; Tan, C. K. I.; Xu, J.; Yan, Q.; Loh, X. J.; Suwardi, A., *Mater. Today Phys.* **2021,** *21*, 100519.
[10] Suwardi, A.; Cao, J.; Zhao, Y.; Wu, J.; Chien, S. W.; Tan, X. Y.; Hu, L.; Wang, X.; Wang, W.; Li, D., *Mater. Today Phys.* **2020,** *14*, 100239.
[11] Gong, Z.; Saglik, K.; Wu, J.; Suwardi, A.; Cao, J., *Nanoscale* **2023,** *15* (45), 18283-18290.
[12] Dong, J.; Suwardi, A.; Tan, X. Y.; Jia, N.; Saglik, K.; Ji, R.; Wang, X.; Zhu, Q.; Xu, J.; Yan, Q., *Mater. Today* **2023**.
[13] Luo, Z.-Z.; Cai, S.; Hao, S.; Bailey, T. P.; Luo, Y.; Luo, W.; Yu, Y.; Uher, C.; Wolverton, C.; Dravid, V. P., *Energy Environ. Sci.* **2022,** *15* (1), 368-375.
[14] Zheng, Y.; Slade, T. J.; Hu, L.; Tan, X. Y.; Luo, Y.; Luo, Z.-Z.; Xu, J.; Yan, Q.; Kanatzidis, M. G., *Chem. Soc. Rev.* **2021,** *50* (16), 9022-9054.
[15] Luo, Y.; Hao, S.; Cai, S.; Slade, T. J.; Luo, Z. Z.; Dravid, V. P.; Wolverton, C.; Yan, Q.; Kanatzidis, M. G., *J. Am. Chem. Soc.* **2020,** *142* (35), 15187-15198.
[16] Xiang, B.; Liu, J.; Yan, J.; Xia, M.; Zhang, Q.; Chen, L.; Li, J.; Tan, X. Y.; Yan, Q.; Wu, Y., *J. Mater. Chem. A* **2019,** *7* (31), 18458-18467.
[17] Biswas, K.; He, J.; Blum, I. D.; Wu, C.-I.; Hogan, T. P.; Seidman, D. N.; Dravid, V. P.; Kanatzidis, M. G., *Nature* **2012,** *489* (7416), 414-418.
[18] Jiang, Y.; Dong, J.; Zhuang, H.-L.; Yu, J.; Su, B.; Li, H.; Pei, J.; Sun, F.-H.; Zhou, M.; Hu, H., *Nat. Commun.* **2022,** *13* (1), 6087.
[19] Jia, N.; Tan, X. Y.; Xu, J.; Yan, Q.; Kanatzidis, M. G., *Acc. Mater. Res.* **2022,** *3* (2), 237-246.
20. Saglik, K.; Tan, X.; Suwardi, A.; Yan, A. Q., *Trans. Tianjin Univ.* **2023**, 1-7.
[21] Saglik, K.; Dong, J.; Zhang, D.; Hsu, T. Z.; Duran, S. S. F.; Cao, J.; Zhu, Q.; Ji, R.; Kai, W. S.; Lang, T. S., *J. Solid State Chem.* **2024**, 124642.
[22] Toberer, E. S.; Zevalkink, A.; Snyder, G. J., *J. Mater. Chem.* **2011,** *21* (40), 15843-15852.
[23] Chen, Z.; Zhang, X.; Pei, Y., *Adv. Mater.* **2018,** *30* (17), 1705617.
[24] Chen, Y.; Gao, Z.; Zhang, F.; Wen, Z.; Sun, X. In *Recent progress in self‐powered multifunctional e‐skin for advanced applications*, *Exploration* Wiley Online Library: **2022**; p 20210112.

[25] Xu, S.; Liu, Y.; Lee, H.; Li, W. In *Neural interfaces: Bridging the brain to the world beyond healthcare*, *Exploration* Wiley Online Library: **2024**; p 20230146.
[26] Yang, D.; Yao, W.; Chen, Q.; Peng, K.; Jiang, P.; Lu, X.; Uher, C.; Yang, T.; Wang, G.; Zhou, X., *Chem. Mater.* **2016,** *28* (6), 1611-1615.
[27] Dou, W.; Spooner, K.; Kavanagh, S.; Zhou, M.; Scanlon, D. O., **2024**.
[28] Lefèvre, R.; Berthebaud, D.; Lebedev, O.; Pérez, O.; Castro, C.; Gascoin, S.; Chateigner, D.; Gascoin, F., *J. Mater. Chem. A* **2017,** *5* (36), 19406-19415.
[29] Shi, W.; Ge, N.; Wang, X.; Wang, Z., J. Phys. Chem. C **2021,** *125* (30), 16413-16419.
[30] Witting, I. T.; Chasapis, T. C.; Ricci, F.; Peters, M.; Heinz, N. A.; Hautier, G.; Snyder, G. J., *Adv. Electron. Mater.* **2019,** *5* (6), 1800904.
[31] Zhang, Y.; Niu, C.; He, H.; Wu, Y.; Rong, M.; Yu, K.; Ren, H., J. Appl. Phys. **2021,** *130* (2). DOI 10.1063/5.0045182.
[32] Ahmad, A.; Zhu, B.; Wang, Z.; Gui, Z.; Wang, W.; Wang, T.; Yu, Y.; Huang, L.; He, J., *Energy Environ. Sci.* **2024,** *17* (2), 695-703.
[33] Pan, Y.; Aydemir, U.; Grovogui, J. A.; Witting, I. T.; Hanus, R.; Xu, Y.; Wu, J.; Wu, C.-F.; Sun, F.-H.; Zhuang, H.-L.; Dong, J.-F.; Li, J.-F.; Dravid, V. P.; Snyder, G. J., *Adv. Mater.* **2018,** *30* (34), 1802016. DOI https://doi.org/10.1002/adma.201802016.
[34] Jang, H.; Abbey, S.; Frimpong, B.; Nguyen, C. V.; Ziolkowski, P.; Oppitz, G.; Kim, M.; Song, J. Y.; Shin, H. S.; Jung, Y. S., *ACS Appl. Mater. Interfaces* **2022,** *14* (1), 1270-1279.
[35] Chen, C.; Shen, D.; Xia, C.; Zhang, Z.; Wang, W.; Zhang, Q.; Chen, Y., *Chem. Eng. J.* **2022,** *441*, 135968.
[36] Wang, W.; Lu, X.; Sun, L.; Luo, J.; Shi, Q.; Ta, N.; Jiang, P.; Bao, X., J. *Mater. Chem. A* **2022,** *10*. DOI 10.1039/D2TA05287C.
[37] Li, C.; Luo, Y.; Li, W.; Yang, L.; Ma, W.; Ma, Z.; Sun, C.; Yang, B.; Wei, Y.; Li, X., *Scripta Mater.* **2024,** *247*, 116090.
[38 Xu, T.; Yakubu Haruna, A.; Ma, Z.; Li, W.; Li, J.; Yubo, L.; Zhang, D.; Yang, J., *Chem. Mater.* **2021,** *33*. DOI 10.1021/acs.chemmater.1c02895.
[39] Saglik, K.; Tan, X. Y.; Dong, J.; Suwardi, A.; Wang, X.; Xu, J.; Zhu, Q.; Liu, H.; Cao, J.; Yan, Q., *Phys. Chem. Chem. Phys.* **2025**. DOI 10.1039/D4CP04219K.
[40] Tan, X. Y.; Dong, J.; Liu, J.; Zhang, D.; Solco, S. F. D.; Sağlık, K.; Jia, N.; You, I. J. W. J.; Chien, S. W.; Wang, X., *Adv. Sci.* **2024**, 2400870.
[41] Cao, J.; Chien, S. W.; Tan, X. Y.; Tan, C. K. I.; Zhu, Q.; Wu, J.; Wang, X.; Zhao, Y.; Yang, L.; Yan, Q., *ChemNanoMat* **2021,** *7* (4), 476-482.
[42] Kahiu, J. N.; Kihoi, S. K.; Lee, H. S., J. Mater. Chem. C **2021,** *9* (36), 12374-12387.
[43] Dadhich, A.; Saminathan, M.; Muthiah, S.; Bhui, A.; Perumal, S.; Rao, M. R.; Sethupathi, K., *ACS Appl. Mater. Interfaces* **2023,** *15* (45), 52368-52380.
[44] Hu, X.; Zheng, S.; Xiong, Q.; Wu, S.; Huang, Y.; Zhang, B.; Wang, W.; Wang, X.; Li, N.; Zhou, Z., *Mater. Today Phys.* **2023,** *38*, 101255.
[45] Feng, B.; Tang, Y.; Lei, J., J. Mater. Sci.: Mater. Electron. **2021,** *32*, 28534-28541.
[46] Yue, L.; Cui, W.; Zheng, S.; Wu, Y.; Wang, L.; Bai, P.; Dong, X., *J. Phys. Chem. C* **2020,** *124* (10), 5583-5590.
[47] Li, F.; Wang, W.; Qiu, X.; Zheng, Z.; Fan, P.; Luo, J.; Li, B., *Inorg. Chem. Front.* **2017,** *4* (10), 1721-1729.
[48] Madavali, B.; Nagarjuna, C.; Dewangan, S. K.; Ahn, B.; Hong, S.-J., *Mater. Today Commun.* **2024,** *40*, 109396. DOI https://doi.org/10.1016/j.mtcomm.2024.109396.
[49] Hong, M.; Lyu, W.; Wang, Y.; Zou, J.; Chen, Z.-G., *J. Am. Chem. Soc.* **2020,** *142* (5), 2672-2681.

[50] Ma, Z.; Luo, Y.; Dong, J.; Liu, Y.; Zhang, D.; Li, W.; Li, C.; Wei, Y.; Jiang, Q.; Li, X., *Adv. Mater.* **2024**, 2407982.
[51] Jiang, B.; Yu, Y.; Cui, J.; Liu, X.; Xie, L.; Liao, J.; Zhang, Q.; Huang, Y.; Ning, S.; Jia, B., *Science* **2021,** *371* (6531), 830-834.
[52] Jiang, B.; Wang, W.; Liu, S.; Wang, Y.; Wang, C.; Chen, Y.; Xie, L.; Huang, M.; He, J., *Science* **2022,** *377* (6602), 208-213.
[53] Wei, Y.; Ma, Z.; Li, W.; Li, C.; Yang, B.; Sun, C.; Gang, S.; Zhang, W.; Long, H.; Li, X.; Jiang, Q.; Zhang, D.; Luo, Y.; Yang, J., *Adv. Funct. Mater.* **2024,** *34* (24), 2313719. DOI https://doi.org/10.1002/adfm.202313719.
[54] Dong, J.; Gao, J.; Yan, Q., *Mater. Lab.* **2023**.
[55] Wang, W.; Liu, S.; Wang, Y.; Jia, B.; Huang, Y.; Xie, L.; Jiang, B.; He, J., *Sci. Adv.* **2024,** *10* (25), eadp4372.
[56] Zhang, Q.; Yuan, M.; Pang, K.; Zhang, Y.; Wang, R.; Tan, X.; Wu, G.; Hu, H.; Wu, J.; Sun, P.; Liu, G.-Q.; Jiang, J., *Adv. Mater.* **2023,** *35* (21), 2300338. DOI https://doi.org/10.1002/adma.202300338.
[57] Wei, T.-R.; Guan, M.; Yu, J.; Zhu, T.; Chen, L.; Shi, X., *Joule* **2018,** *2* (11), 2183-2188.
[58] Borup, K. A.; De Boor, J.; Wang, H.; Drymiotis, F.; Gascoin, F.; Shi, X.; Chen, L.; Fedorov, M. I.; Müller, E.; Iversen, B. B., *Energy Environ. Sci.* **2015,** *8* (2), 423-435.
[59] Komisarchik, G.; Gelbstein, Y.; Fuks, D., *Intermetallics* **2017,** *89*, 16-21.
[60] Shuai, J.; Mao, J.; Song, S.; Zhu, Q.; Sun, J.; Wang, Y.; He, R.; Zhou, J.; Chen, G.; Singh, D. J., *Energy Environ. Sci.* **2017,** *10* (3), 799-807.
[61] Snyder, G. J.; Snyder, A. H.; Wood, M.; Gurunathan, R.; Snyder, B. H.; Niu, C., *Adv. Mater.* **2020,** *32* (25), 2001537. DOI https://doi.org/10.1002/adma.202001537.
[62] Snyder, G. J.; Pereyra, A.; Gurunathan, R., *Adv. Funct. Mater.* **2022,** *32* (20), 2112772.
[63] Zhu, T.; Hu, L.; Zhao, X.; He, J., *Adv. Sci.* **2016,** *3* (7), 1600004.
[64] Ma, Z.; Luo, Y.; Li, W.; Xu, T.; Wei, Y.; Li, C.; Haruna, A. Y.; Jiang, Q.; Zhang, D.; Yang, J., *Chem. Mater.* **2022,** *34* (19), 8959-8967. DOI 10.1021/acs.chemmater.2c02344.
[65] Kang, S. D.; Snyder, G. J., *arXiv preprint arXiv:1710.06896* **2017**.